Scaling and Prediction of Transfer Functions in Lean Premixed H 2 /CH 4 - Flames

Article *in* Combustion and Flame · January 2020

DOI: 10.1016/j.combustflame.2020.01.045

Scaling and Prediction of Transfer Functions in Lean Premixed H_2/CH_4-Flames

Eirik Æsøy[a], José G. Aguilar[a], Samuel Wiseman[a], Mirko R. Bothien[b], Nicholas A. Worth[a], James R. Dawson[a]

[a] *Department of Energy and Process Engineering, Norwegian University of Science and Technology, Trondheim N-7491, Norway*
[b] *Ansaldo Energia, Baden, Switzerland*

Abstract

Features of the flame transfer function (FTF) are characterized for turbulent, non-swirled, bluff body stabilized "M" flames for different hydrogen and methane blends including pure hydrogen flames. An increase in the cut-off frequency of the FTF is observed for increasing hydrogen concentration. Modulations in the form of peaks and troughs in the gain and the phase were also observed and are shown to be caused by the interaction of two different flow disturbances, acoustic and convective, originating upstream of the flame. The first mechanism is due to the acoustic velocity fluctuations imposed at the base of the flame. A Strouhal number scaling based on the flame height and bulk velocity is shown to collapse the phase slopes and the cut-off frequencies. The second mechanism is shown to be due to vortex shedding from the grub screws used to align the bluff body in the inlet pipe. The associated convective time-delay is used to define a second Strouhal number which collapses the modulations in the gain and phase.

A model is developed that separately considers the impulse response of each mechanism and is interpreted as a distribution of time lags between velocity fluctuations and the unsteady heat release rate. The distributed time lag (DTL) model consists of two distributions that are shown to capture all the features of the FTFs. The distributions show that the acoustic and convective mechanisms behave as a low pass filter and band pass filter respectively. This results in a band of frequencies where they interact through superposition driving fluctuations of heat release rate. Similar interactions are shown to exist in the forced cold flow revealing that they are of hydrodynamic origin. Further, the band of frequencies are shown to be centered around the natural shedding frequency of the grub screws appearing as peaks in the unforced energy spectra of the velocity at the dump plane.

Finally, a generalized model which takes as an input the bulk velocity, flame height and a geometric parameter is derived assuming a linear dependency of the DTL parameters. The model is shown to predict the behaviour of the FTFs relatively well and can potentially be used to analyse regions in the operating conditions map which have not been experimentally tested.

Keywords: thermoacoustics, flame transfer function, distributed time lag model, turbulent premixed flame, hydrogen

1. Introduction

Hydrogen fired gas turbines for power generation can potentially play a crucial role in large-scale decarbonisation. This is because hydrogen can be produced using excess energy from renewable energy sources or from reforming from natural gas combined with capture and storage of carbon dioxide. However, the higher flame speeds of hydrogen mixtures introduces new flame dynamics that may lead to thermoacoustic oscillations in addition to other flame stability issues such as flashback.

Thermoacoustic instabilities can arise whenever there is feedback from the unsteady heat release into the acoustic field of the surrounding geometry [1]. In order to predict and control these instabilities, a model of the combustion system is required. Typically, these models are built considering the acoustic characterization of the chamber, boundary conditions and a transfer function that relates the acoustic excitation to the unsteady heat release. The latter occurs because heat sources, such as flames, are volume sources which act as acoustic monopoles.

As it provides closure to the thermoacoustic feedback loop, flame transfer function (FTF) analysis is a core subject of research in thermoacoustics. FTFs can be obtained experimentally [2, 3, 4, 5], via high fidelity numerical simulations [6], or using theoretical models [7, 8, 9, 10]. Owing to the weak acoustic amplification of the pressure and/or density fluctuations across a flame, the FTF is usually assumed to be proportional to the velocity fluctuations only and is by definition independent of the forcing level. This corresponds to the case where there is a linear relationship between the normalized heat release fluctuations and the normalized velocity fluctuations.

The time-lag nature of thermoacoustic instabilities is commonly expressed using single time-lag (STL) models as FTFs, such as the $n-\tau$ model introduced by Crocco [11]. These models have an impulse response function (IRF), where the local response is both: amplified by a factor of n, and delayed τ seconds. However, this representation is only valid at low frequencies where the flame is considered compact with respect to the acoustic and convective wavelengths. At moderate frequencies, STL formulation has been shown incapable of capturing the spatial dispersion that arises due to the presence of convective phenomena [7]. In other words STL formulation cannot capture cut-off frequency behaviour. To circumvent this limita-

*Corresponding author.
Email address: eirik.asoy@ntnu.no ()

tion Sattelmayer [12] introduced the distributed time lag (DTL) formulation. In this formalism, the FTF is computed from the IRF obtained from the probability density function (PDF) of time-delays. This analysis was extended in Polifke et al. [13] to handle arbitrary shapes of the PDF enabling the FTF to capture cut-off frequency behaviour. Furthermore, there are some premixed flames, whose FTFs also display excess gain (Gain > 1) at non zero frequencies ($f > 0$) [14]. Huber and Polifke [15] discussed that for the FTF to display excess gain the IRF must allow for negative values. This was shown by Blumenthal et al. [16] to be the case in some laminar flames. In most of the aforementioned studies, the FTF is due the mechanisms that occur around one dominant time scale. In these cases the FTFs can be well represented by a single DTL model. However, there are situations in which there are two mechanisms with very different time scales responsible for the fluctuations in the heat release rate. In such cases it is convenient to use the sum of two DTL models to approximate the IRF. For instance, Schuermans et al. [17] used this approach to model the mechanisms due to equivalence ratio fluctuations and vorticity fluctuations in a full scale gas turbine burner mounted in an atmospheric test rig.

The most common feature of a FTF is that the flame behaves as a low-pass filter [7] however other features can appear strongly influenced by the shape of the flame [3]. In the case of so-called "M" flames, particular features include the presence of peaks and troughs (also referred to as modulations), such as those appearing in the studies of swirl stabilized flames [5, 18, 19, 20]. Using premixed flames Komarek and Polifke [19] demonstrated that the peaks and troughs shift in frequency when the position of the swirler is changed. The same effect was achieved by Polifke [18] by changing the location of the fuel injection point when equivalence ratio oscillations are present. On a different configuration Palies et al. [21] identified the peaks and troughs to be the interaction between two different unsteady heat release mechanisms: swirl number fluctuations and vortices shed from the bluff-body. In a series of more recent experiments [22, 23, 24] it was demonstrated that the levels of swirl number fluctuations observed at both the peaks and the troughs of the FTF were the result of the axial and angular velocity fluctuations being in or out of phase. Gatti et al. [23] further showed that the FTF of a non-swirling flame, and a swirling flame without a center rod, did not exhibit peaks or troughs.

In the present paper FTFs are measured for a variety of non-swirling flames stabilized on a bluff-body over a wide range of hydrogen/methane mixtures with "M" flame shape. The experimental FTFs show that the modulations can also occur under these conditions. Scaling laws, similar to those used by Alemela et al. [25], are deduced to collapse the cut-off frequency and the modulations in the gain and the phase of the measurements. The time scales derived are similar to those identified in [26] where the flame was subject to interference between vortical and acoustic disturbances. The data is compared against a double DTL model, which includes a modulating term that allows for excess gain to be modelled. It is shown that the modulations in the FTF are caused by the constructive and destructive interference between the acoustic velocity and vortex shedding originating from the geometry upstream. Each of these mechanisms are also shown to act on the flame with different mean time-delays. Using these considerations a generalized FTF model is derived which takes as an input the bulk velocity, flame length and a geometric parameter.

2. Experimental set-up and methods

2.1. Experimental set-up

Figure 1 shows a schematic of the experimental set-up. The burner used in these experiments consists of a single sector rig. The injector geometry is identical to the injectors used in the annular combustor of [27, 28] but without swirlers. The burner has a circular quartz combustion chamber of inner diameter $d_q = 44$ mm, that enables optical access and it is open to atmospheric conditions. The length of the quartz tube can be changed to avoid self excited instabilities during FTF measurements. Two lengths $L_q = 80$ mm and 55 mm are used for these measurements. The combustor is operated with different mixtures of hydrogen, methane and air. The flow rates are controlled by Alicat mass flow controllers (MFC's) and the fluid bulk velocity $\bar{u}$ at the burner dump plane and in the pipe $\bar{u}_p$ are computed from the volume flow rate. The air and fuels are mixed in the feeding lines approximately a meter before entering the bottom of the plenum section to ensure that the mixture is fully premixed. In the plenum section, the gas expands, and flows through a set of honeycombs and perforated plates before it contracts and passes through a pipe of diameter $d_p = 19$ mm. The flame anchors on a bluff body ($d_b = 13$ mm) with blockage ratio of 47%, supported by a center rod ($d_r = 5$ mm) located at the pipe exit. The rod is held in place by three grub screws ($d_g = 4$ mm) at a distance of $L_g = 45$ mm from the dump plane. On the side wall of the plenum, two Monacor KU-516 (75W, 16Ω) horn drivers are attached at the end of two stand off tubes for longitudinal acoustic forcing. The speakers are powered by QTX Sound PRO1000 power amplifiers and controlled by an Aim-TTi TGA1244 40 MHz signal generator (SG). The signal from the SG p_{ref} is sampled as a common reference for cross spectral analysis of pressure, heat release, and velocity oscillations. To characterize the cold flow a Hot Wire Anemometer (HWA) is used at six locations L_{1-6} in the pipe. The velocity magnitude u_{hw} across a single wire (55P11) of diameter 5 µm and length 1.25 mm is measured using a StreamLine pro. Throughout the paper a cylindrical coordinate system (x, r, θ) is used with the origin placed at the center of the bluff body.

2.2. Operating conditions

Measurements were carried out for a range of thermal powers P, bulk velocities $\bar{u}$, equivalence ratios Φ, and hydrogen contents in terms of power fraction P_{H} (or the equivalent volume fraction V_H) computed as:

$$P_{\mathrm{H}} = \frac{P_{\mathrm{H_2}}}{P_{\mathrm{H_2}} + P_{\mathrm{CH_4}}}, \qquad V_{\mathrm{H}} = \frac{V_{\mathrm{H_2}}}{V_{\mathrm{H_2}} + V_{\mathrm{CH_4}}}, \tag{1}$$

where $P_{\mathrm{H_2}}$ and $P_{\mathrm{CH_4}}$ are the thermal powers from hydrogen and methane, and $V_{\mathrm{H_2}}$ and $V_{\mathrm{CH_4}}$ are the volume flow rates of hydrogen and methane. The 25 cases are summarized in Table 1. All

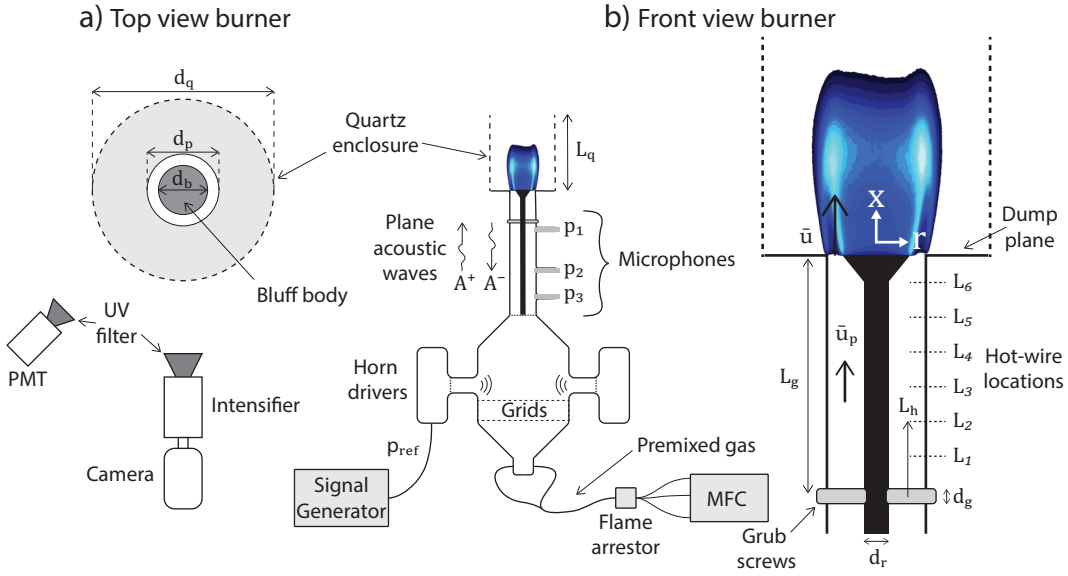

Figure 1: Schematic of the experimental set-up. a) Top view of the burner showing the optical arrangement with the photo multiplier tube and camera. b) Front view of the set-up showing MFCs, signal generator, plenum, horn drivers, microphones, combustion chamber, and a zoomed view of the burner showing the pipe, bluff body, grub screws, combustion chamber, and the locations of the hot-wire used for the cold flow measurements.

these operating points correspond to "M" -flames (similar to the flame shown in Figure 3), where the flame is stabilized both on the inner and outer shear layers near the burner lip. The operating conditions are divided into seven groups which correspond to cases where two parameters are held constant while the rest are changed. These operating conditions are chosen to show the difference in flame dynamics for a similar flame shape.

Table 1: Operating conditions in terms of thermal powers P, bulk velocities $\bar{u}$, equivalence ratios Φ, hydrogen power fraction P_H, and hydrogen volume fraction V_H for FTF measurements of "M" -flames.

P_H	V_H	$\bar{u}$ [m/s]	P [kW]	Φ	Case
1.0	1.0	12.8 – 51.3	3 – 12	0.4	1-9
1.0	1.0	30	7 – 9.8	0.4 – 0.6	10-12
1.0	1.0	23.4 – 19.4	5.47	0.4 – 0.5	13-14
0.3	0.57	8.6 – 31.7	3 – 11	0.7	15-19
0.3	0.57	17.9	7	0.8	20
0.3 – 0.4	0.57 – 0.67	20	7	0.7	21-23
0.8 – 1.0	0.92 – 1.0	30	7	0.4	24-25

2.3. Flame response from global chemiluminescence

The flame response is measured by the spatially integrated heat release rate Q. This is tracked by measuring radiation emitted from OH* radicals, using a photo multiplier tube (PMT) equipped with a UV band pass filter with 310 nm center wave length and a half width of 10 nm. Since we are only considering fully premixed flames, the PMT signal $I(t)$ is assumed to be proportional to the global heat release rate following the example of numerous previous studies [7, 29, 30, 31]. Hence, relative fluctuations, $Q'/\bar{Q}$, are evaluated from the time-series of $I(t)$ from the PMT.

The velocity fluctuations at the burner exit are computed using the multiple microphone method (MMM) [32]. For this purpose three (Kulite XCS-093-05D) microphones located at different axial locations in the inlet pipe are used to measure time-series of pressure (p_1, p_2, and p_3). A cross power spectral analysis is used to estimate the amplitude and phase of each signal p'_{1-3} and Q', correlated with the excitation signal p_{ref}, i.e., the phase is computed relative to p_{ref}. The amplitude and phase of each signal, e.g., Q', is expressed as a complex number and is computed by:

$$\hat{Q}(f_e) = \left.\frac{\Gamma(p_{\mathrm{ref}}, Q')}{\sqrt{\Gamma(p_{\mathrm{ref}}, p_{\mathrm{ref}})}}\right|_{f_e}, \qquad (2)$$
$$\Gamma(p_{\mathrm{ref}}, Q') = \mathcal{F}(p_{\mathrm{ref}})\mathcal{F}(Q')^*,$$

where the cross power spectral density (CPSD), Γ, is computed as the product of the Fourier transforms $\mathcal{F}$ of each signal respectively. Hatted quantities ($\hat{}$) denote a fluctuation in frequency space. The excitation signals are harmonic, hence the signal response is estimated as the complex value at the excitation frequency f_e. Segments of the time-series of $p'_1(t)$, $Q'(t)$, and p_{ref} are plotted in Figure 2b. Figure 2a shows the spectra of the heat release rate computed by Equation 2 at f_e = 950 Hz.

Assuming 1D acoustics and a low mach number, the acoustic pressure and velocity propagate only in the axial direction and are expressed by:

$$\hat{p}(x) = A^+ \exp(-jkx) + A^- \exp(jkx), \qquad (3)$$
$$\hat{u}(x) = \frac{1}{\bar{\rho}\bar{c}}\left(A^+ \exp(-jkx) - A^- \exp(jkx)\right), \qquad (4)$$

where A^+ and A^- are the amplitude and phase (Riemann invariants) of the upstream and downstream propagating acoustic

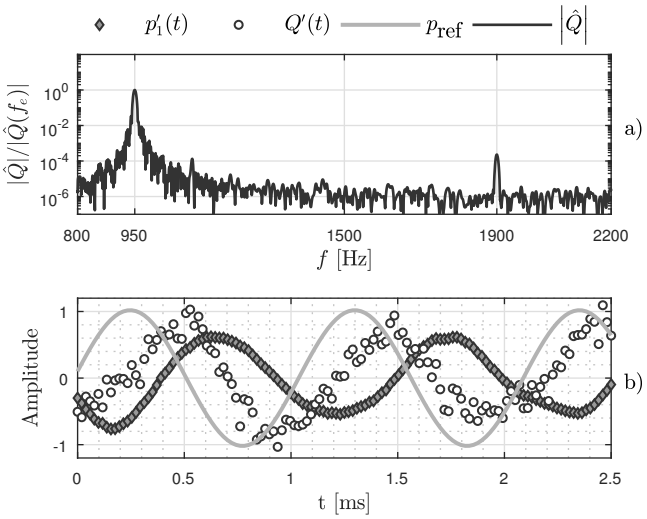

Figure 2: Amplitude spectra of $\hat{Q}$ and corresponding time-series $p_1'(t)$, $Q'(t)$, and p_{ref} at excitation frequency f_e = 950 Hz. The time series in b) are normalized by the amplitudes estimated by Equation 2.

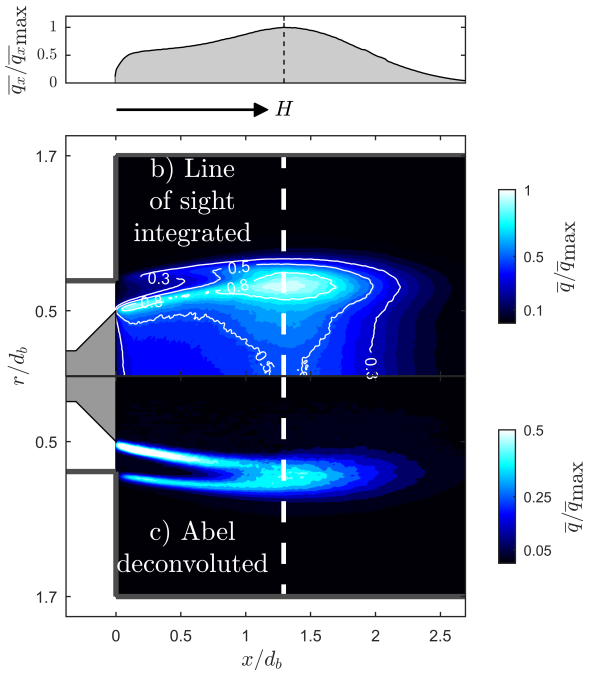

Figure 3: Images of the mean flame for case 5 (P = 7 kW, P_{H} = 1, and Φ = 0.4). a) Stream-wise distribution of heat release rate. b) Line of sight integrated heat release rate. c) Planar heat release rate computed by a 3 point Abel deconvolution algorithm. All images are normalized by the maximum intensity.

waves, $\bar{\rho}$ is the fluid density, $\bar{c}$ is the speed of sound, and k is the spatial wave-number. The wave-number is given by $k = \omega/\bar{c}$, where $\omega = 2\pi f$ is the angular frequency. The amplitude and phase of the microphone signals ($\hat{p}_{1-3}$), are used to compute A^+ and A^- which then are used to reconstruct the acoustic pressure and velocity fields in the tube. Hence, $\hat{u}$ can be evaluated at the burner exit, relating the heat release fluctuations to the acoustic velocity fluctuations at the burner dump plane.

The relationship between $\hat{u}$ and $\hat{Q}$ is described by the flame transfer function (FTF) expressed by:

$$\mathrm{FTF}(\omega) = \frac{\hat{Q}/\bar{Q}}{\hat{u}/\bar{u}}. \tag{5}$$

At low forcing amplitudes the FTF is independent of the forcing level $|\hat{u}|/\bar{u}$ [33]. Discrete points of the FTF are measured using $|\hat{u}|/\bar{u} = 0.04$ at a range of frequencies $f_e = [200 - 2200]$ Hz. At each frequency time-series of pressure and chemiluminescence are recorded in 10s intervals at a sampling rate of f_s = 51.2 kHz. This corresponds to 5.12×10^5 samples which are binned into 40 separate time-series. Each of the time series has a length of 250 ms which correspond to more than 50 cycles at the lowest frequency.

2.4. High-speed imaging and flame shape

The spatial distribution of normalized heat release rate, $q'(x, r, t)/\bar{q}(x, r)$, is measured by high-speed imaging of the flame. The measurement is line of sight integrated (similar to the PMT), and $q'/\bar{q}$ is obtained in the same way as $Q'/\bar{Q}$. The total heat release rate is retrieved by integrating the spatially distributed heat release: $Q'/\bar{Q} = \int_A q'/\bar{q}\ \mathrm{d}A$ over the camera field of view, A.

The equipment used is a Phantom V2012 high-speed camera equipped with a LaVision IRO high-speed two-stage intensifier, fitted with a Cerco 2178 UV lens 100F/2.8 and a UV band pass filter with 310 nm center wave length and a half width of 10 nm.

The mean spatial distribution of heat release rate $\bar{q}$ is used to compute the mean flame shape and corresponding flame height H. Figure 3b shows the upper half of $\bar{q}$ in the $x - r$ plane, obtained from averaging 2000 chemiluminescence images of the unforced flame. Figure 3c, is computed by a three point Abel deconvolution algorithm [34] and shows the radial profile of the heat release rate. The image intensity is normalized by the maximum intensity ($\bar{q}_{\mathrm{max}}$). Figure 3a shows the stream wise intensity profiles of $\bar{q}$, integrated in the radial direction:

$$\bar{q}_x(x) = \int_0^\infty \bar{q}\ \mathrm{d}r. \tag{6}$$

The location where $\bar{q}_x$ is maximum indicates the flame length H. The flame length is shown with a dashed line. From Figure 3c, one can see that the flame anchors on both the inner and outer burner lips forming the characteristic "M" shape.

3. Results

Figure 4 shows FTFs measurements of two fuel mixtures. The first mixture is an H_2/CH_4 blend at P_{H} = 0.3, with equivalence ratio, Φ = 0.7, at a range of thermal powers $P = [3 - 7]$ kW. The second mixture is pure H_2, P_{H} = 1, with equivalence ratio, Φ = 0.4, at a range of thermal powers $P = [4 - 12]$ kW. The FTF is plotted using $\mathrm{FTF} = G\exp(j\theta)$, where G is the gain and θ is the phase. Log-log plots of the gain are shown on the left, and the phase is plotted on the right of the figure. The

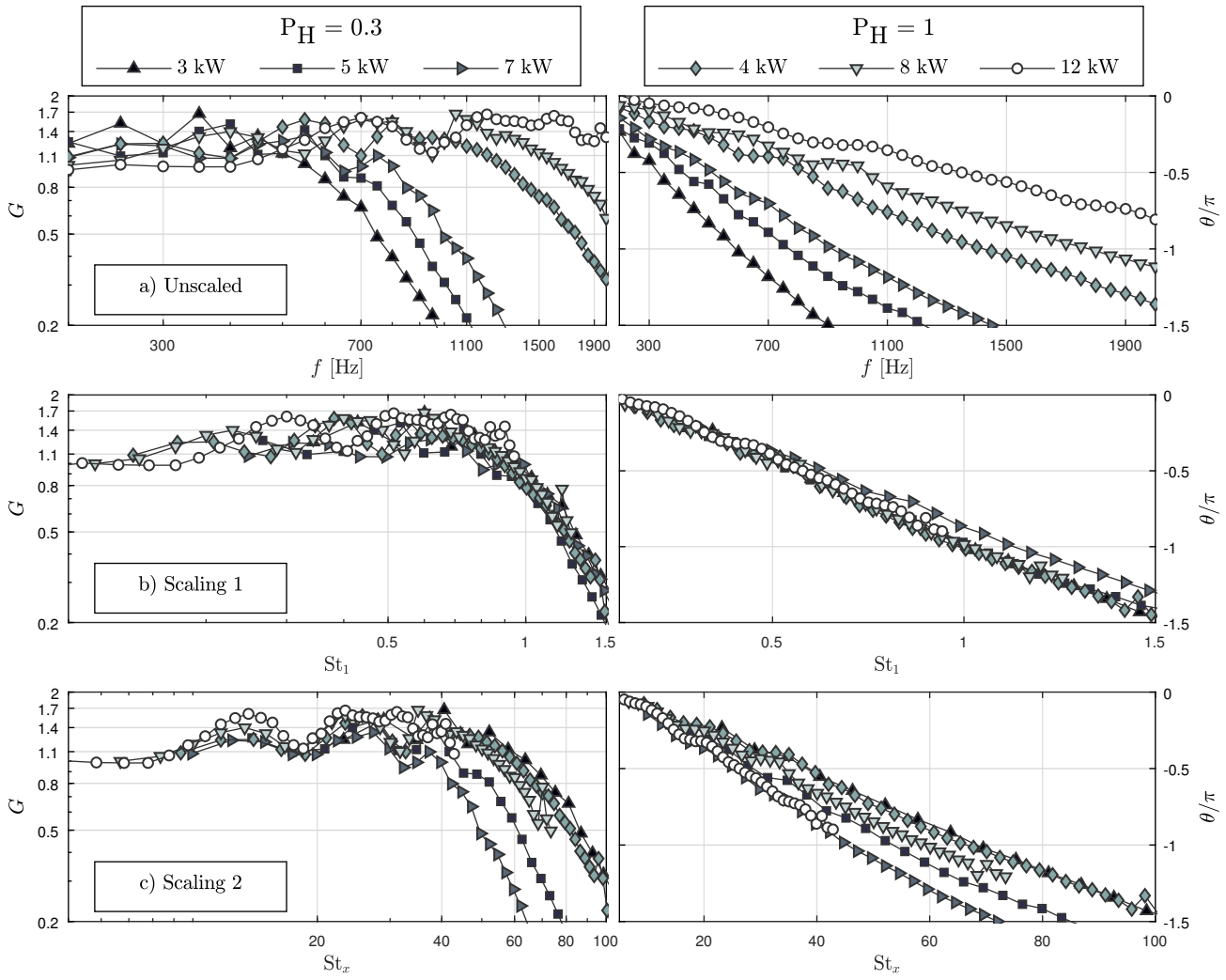

Figure 4: Experimental FTFs for "M" -flames at different thermal powers: $P = [3-7]$ kW for $P_H = 0.3$ at $\Phi = 0.7$, and $P = [4-12]$ kW for $P_H = 1$ at $\Phi = 0.4$. a) Gain and phase plotted against frequency. b) Plotted against reduced frequency St_1. c) Plotted against reduced frequency St_x.

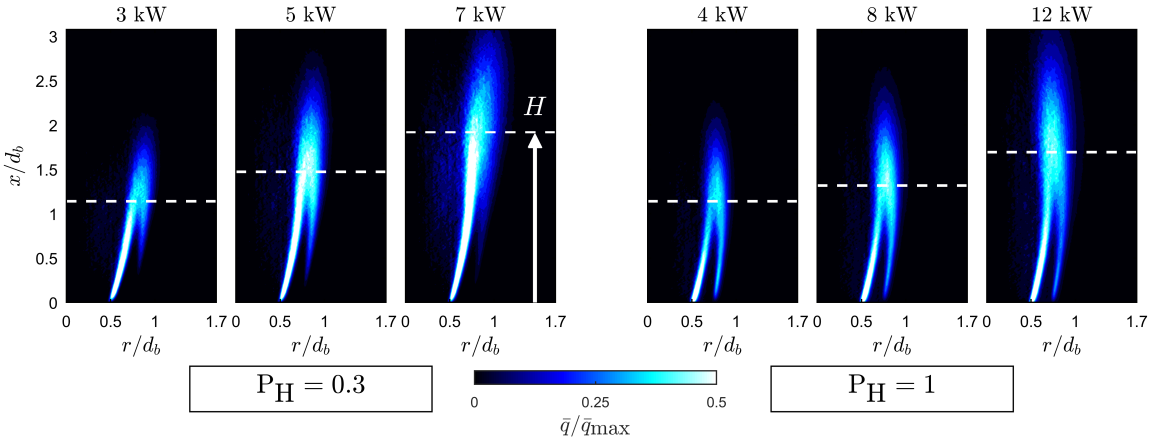

Figure 5: Planar flame images of the unforced flame at different thermal powers: $P = [3-7]$ kW for $P_H = 0.3$ at $\Phi = 0.7$, and $P = [4-12]$ kW for $P_H = 1$ at $\Phi = 0.4$. The flames correspond to the FTFs shown in Figure 4. All flames have a characteristic "M" -shape and the intensity is normalized by the maximum intensity $\bar{q}_{max}$.

gain plots highlight the low-pass filter behaviour where an exponentially decaying gain appears as a line with negative slope at high frequencies. The phase is plotted in a linear scale to highlight the time-delayed response of the flame as indicated by the approximately constant slope. It is evident that the cut-off frequency increases and the time-delay decreases with thermal power. The pure hydrogen mixture exhibits a significantly higher cut-off frequency and a slower time delay when compared to the H_2/CH_4 mixture at similar thermal powers. Furthermore, one can see that before the cut-off frequency, the gain modulates around unity and the phase is deviating from a straight line by the same type of oscillations (see Figure 11b for individual plots of some of the cases). The planar flame images in Figure 5, correspond to each of the FTFs in Figure 4a, and show that hydrogen flames are stabilized as an "M" flame for a large range of thermal powers. The flame height is denoted by the dashed line. By increasing the thermal power and thus the bulk velocity, the turbulent flame speed also increases, albeit less than the bulk velocity. This results in longer flames as the flame height is primarily controlled by the balance between turbulent flame speed and bulk velocity.

3.1. FTF measurements for pure hydrogen "M" -flames

Some features of the FTF collapse when scaled by appropriate Strouhal numbers. Figure 4b shows that when the frequency in the FTFs of Figure 4a is non-dimensionalized by a time-scale based on the flame height and the bulk velocity, $\tau_1 = H/\bar{u}$, such that $\mathrm{St}_1 = f\tau_1$ the cut-off characteristics in the gain and the phase slopes collapse. The periodic nature of the peaks and troughs in the low frequency gain and phase curves suggests that there is another Strouhal number, say St_x, which collapses the modulations as shown in Figure 4c. The nature of the second time-delay is analysed in section 3.4. Given that different features of the FTF scale with different Strouhal numbers, one can conclude that the system is governed by two distinct time scales. Similar observations were made in swirling flames [21, 22, 23, 24] where it was shown that two different time-scales affected the FTF, one corresponding to the acoustic velocity disturbances at the burner exit and the other to vorticity waves produced by the swirler vanes.

In the following sections an in depth characterization of the time-delays is performed. First by adopting a distributed time lag model to extract the actual time-delays and then analysing the corresponding nature of the disturbances.

3.2. Distributed Time-lag model

The simplest time lag model used to relate the velocity fluctuations with the flame response is the $n-\tau$ model, originally proposed by Crocco [11]:

$$\frac{Q'(t)}{\bar{Q}} = n\frac{u'(t-\tau)}{\bar{u}}. \tag{7}$$

Here n is the interaction index, and τ is the time-delay. This representation is only valid in the low frequency range, where the flame can be treated as a compact element with respect to the acoustic and convective wavelengths.

This is not the case for the flames and frequencies considered in this paper. At moderate frequencies, disturbances that convect with the mean flow velocity can have a significant effect on the flame. In this case, the flame response is better represented by a distributed time-lag model. Using CFD Polifke et al. [13] computed the probability density function of time delays, also interpreted as the impulse response function $h(t)$ and then approximated it analytically using a Gaussian distribution with standard deviation σ:

$$h(t) = \frac{1}{\sigma\sqrt{2\pi}}\exp\left(-\frac{(t-\tau)^2}{2\sigma^2}\right). \tag{8}$$

In order to capture excess gain, i.e., gain above unity ($G > 1$) at nonzero frequency ($f > 0$) Komarek and Polifke [19] used several distributions with opposite signs. In order to achieve the same effect we extend the model to include an amplitude g and a modulating term with frequency β. The advantages of using the modulating term are twofold:

1. It allows the impulse response function h to become negative and therefore it is useful to model excess gain in the FTF (see Figure 6).
2. If such a distribution is used to model a phenomenon with a preferred frequency, β represents this explicitly (as will be shown in section 3.5).

Under these considerations the impulse response for a single time lagged distribution is given by:

$$h(t) = \frac{g}{\sigma\sqrt{2\pi}}\exp\left(-\frac{(t-\tau)^2}{2\sigma^2}\right)\cos\left(\beta(t-\tau)\right). \tag{9}$$

The relationship between the unsteady heat release fluctuations and the velocity fluctuations is given by the convolution of the latter with the impulse response function:

$$\frac{Q'(t)}{\bar{Q}} = \frac{(h * u')(t)}{\bar{u}}, \tag{10}$$

$$= \int_{-\infty}^{\infty} h(\tau)\frac{u'(t-\tau)}{\bar{u}}\,\mathrm{d}\tau. \tag{11}$$

In the frequency domain this can be rewritten as:

$$\frac{\hat{Q}(\omega)/\bar{Q}}{\hat{u}(\omega)/\bar{u}} = \hat{h}(\omega), \tag{12}$$

where $\hat{h}(\omega)$ is the associated transfer function given by:

$$\hat{h}(\omega) = \frac{g}{2}\left(\exp\left(-\frac{1}{2}(\omega-\beta)^2\sigma^2\right) + \exp\left(-\frac{1}{2}(\omega+\beta)^2\sigma^2\right)\right)\mathrm{e}^{-j\omega\tau}. \tag{13}$$

This formulation can be used to describe the mechanisms responsible for the unsteady heat release fluctuations that occur around a single time scale (τ). When there are two different time scales, as the analysis in section 3.1 suggests, it is convenient to use two distributed time lag models [17]. Therefore the full FTF expressed as $\mathrm{DTL_T}(\omega)$ is given by:

$$\mathrm{DTL_T}(\omega) = \mathrm{DTL_1} + \mathrm{DTL_2}, \tag{14}$$

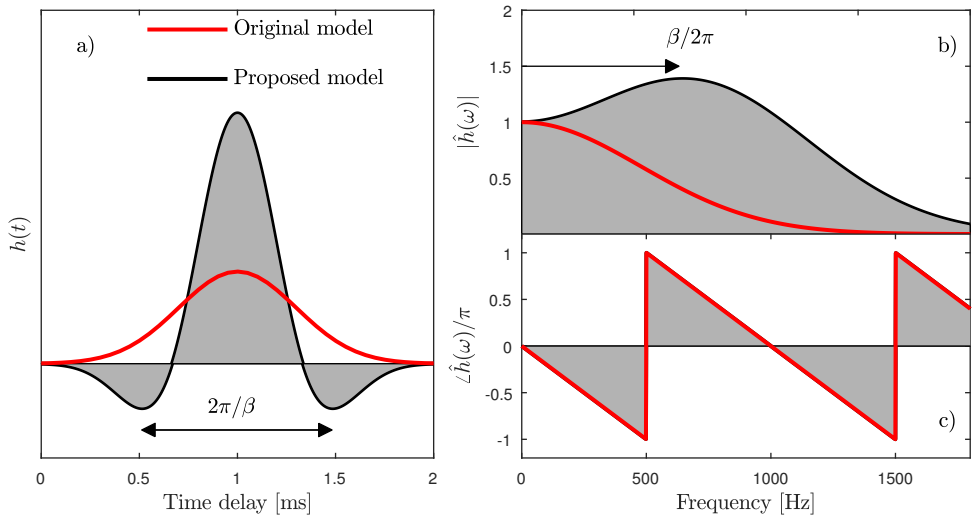

Figure 6: a) Impulse response function $h(t)$, with mean time-delay $\tau = 1$ ms and a modulation frequency of $\beta/(2\pi) = 700$ Hz. This corresponds to a modulation wavelength of 1 ms. b) Transfer function $\hat{h}(\omega)$ displaying excess gain at $f = \beta/(2\pi)$.

where

$$\mathrm{DTL}_i = E_i^+ + E_i^-, \tag{15}$$

$$E_i^{\pm} = \frac{g_i}{2}\exp\left(-\frac{1}{2}(\omega \pm \beta_i)^2\sigma_i^2 - j\omega\tau_i\right). \tag{16}$$

3.3. Estimation of the DTL model parameters

Having developed the DTL model, the next step is to compute the model parameters (g_i, β_i, σ_i and τ_i) that best fit the experimental FTFs. This is performed using a nonlinear least squares (NLS) optimization routine which minimizes the difference between the DTL model and the experimental measurements. The procedure is as follows:

1. The measurements are fitted to a DTL model consisting of one distribution. Hence, the model parameters g_1, σ_1, β_1, and τ_1 are computed while g_2, σ_2, β_2, and τ_2 are set to zero.
2. The measurements are fitted to a DTL model consisting of two distributions. The first distribution takes the values computed in the previous step, and only the model parameters g_2, σ_2, β_2, and τ_2 are computed.
3. The measurements are fitted to a DTL model consisting of two distributions, where all the model parameters are fitted simultaneously and physical constraints are imposed.

The main challenge associated with the NLS approximation is that it easily gets trapped in local minima which may not necessarily be the global minima. This is important for steps 1 and 2 (step 3 takes as initial guesses the values computed in steps 1 and 2). Therefore one may prefer to use a global minimization approach as applied by genetic algorithms. However, the NLS algorithm is favored in this paper because, as will be shown in the following sections, a careful analysis of the features of the FTFs can provide good initial estimates of the model parameters.

3.3.1. Parameter estimation for the first distribution

When dealing with a single distribution, one can divide the model parameters into gain (g_1, σ_1, β_1) and phase (τ_1) parameters. Good estimations for the gain parameters can be obtained by inspection of the FTF, by considering $G_m = \max(G)$:

$$g_1 \approx 2G_m, \qquad \beta_1 \approx \omega\Big|_{G=G_m}, \qquad \sigma_1 \approx \frac{3}{\omega\big|_{G=G_m/100} - \beta_1}.$$

Figure 4b shows that using a Strouhal number based on the time-delay $\tau_1 = H/\bar{u}$ collapses the cut off frequency characteristics and the phase slopes of 5 curves. However, instead of taking this as granted, the initial guess for the time-delay is given as the slope of the phase computed using linear regression[1]. The same figure also shows that the phase at the origin is not zero (which is a feature of the DTL model). This can be caused by systematic measurement errors. In order to get a better estimate of the phase slopes a small phase offset (θ_0) is added to the model such that $\exp(-j\omega\tau_i) \rightarrow \exp(-j(\omega\tau_i + \theta_0))$. Note that the offset needs to be the same for both distributions. The initial estimation for this offset is taken to be zero.

3.3.2. Parameter estimation for the second distribution

In Figure 4c it is shown that the modulations collapse with a, yet unknown, Strouhal number. This suggests that a detailed analysis of the modulations can provide accurate estimations for the model parameters of the second distribution. Having computed the model parameters of the first distribution, the modulations in the gain[2] are extracted by taking the difference between the gain of the experimental data (G_{exp}) and the gain of the DTL model with a single distribution (G_{DTL_1}):

$$\Delta G = G_{\mathrm{exp}} - G_{\mathrm{DTL}_1}. \tag{17}$$

[1] It will be shown later in the paper that the slope of the first distribution is exactly τ_1.

[2] This analysis is carried out with the modulations in the gain, the same analysis giving similar results can be done with the phase modulations but is not shown here for brevity.

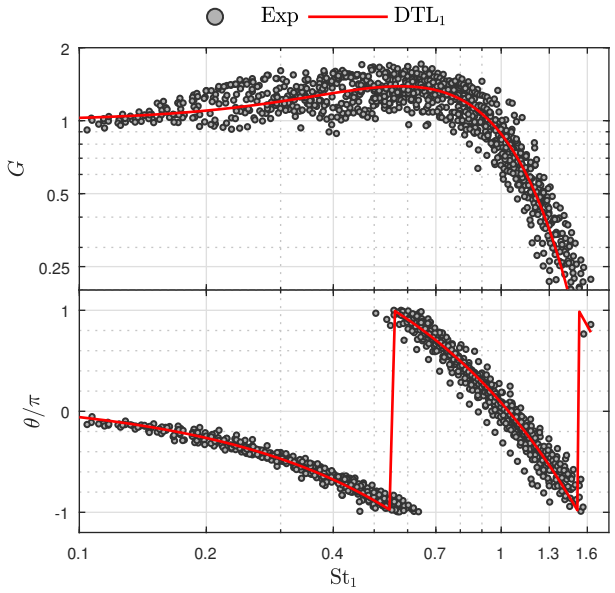

Figure 7: Experimental FTFs of cases 1-25 scaled by St_1. The solid line is the DTL model using a single distribution. Notice that the phase slopes and the cut off frequency characteristics collapse. The phase offset of the red curve is $\theta_0/(2\pi) = 0.075$.

The modulations appear only in a band of frequencies, thus the part of the signal out of this band is discarded. This gives an estimate for β_2 which is approximately the center of the band. The width of the band is roughly $6/\sigma_2$ and the amplitude of the modulations are twice g_2. The resulting signal (shown later in Figure 8) closely resembles a sinusoidal curve where the peaks and troughs can be interpreted as the frequencies at which the mechanisms of different time scales have constructive and destructive interference respectively.

The periodicity of this curve is linked to the second time-delay. Recall that the magnitude of the addition of two complex numbers $z_1 = r_1 e^{j\phi_1}$ and $z_2 = r_2 e^{j\phi_2}$ is given by:

$$|z_1 + z_2| = \sqrt{r_1^2 + r_2^2 + 2r_1 r_2 \cos(\phi_1 - \phi_2)}. \tag{18}$$

The peaks of the signal will appear whenever $\phi_1 - \phi_2 = 2\pi n$, with $n \in \mathbb{Z}$. Considering that $\phi_2 = -\omega\tau_2 - \theta_0$ and $\phi_1 = -\omega\tau_1 - \theta_0$ then it is possible to find the frequency of the nth peak:

$$\omega_n = \frac{2\pi n}{\tau_2 - \tau_1}. \tag{19}$$

Using the wavelength between two consecutive peaks $\lambda = \omega_{n+1} - \omega_n$ one finds an estimate for the second time-delay:

$$\begin{aligned} \tau_2 &= \tau_1 + \frac{2\pi}{\lambda} \\ &= \tau_1 + \tau_3. \end{aligned} \tag{20}$$

3.3.3. Physical constraints for the final DTL model

Using mass and energy conservation laws Polifke and Lawn [8] show that in the low frequency limit, $\omega \to 0$, the FTF approaches unity for perfectly premixed flames. This translates

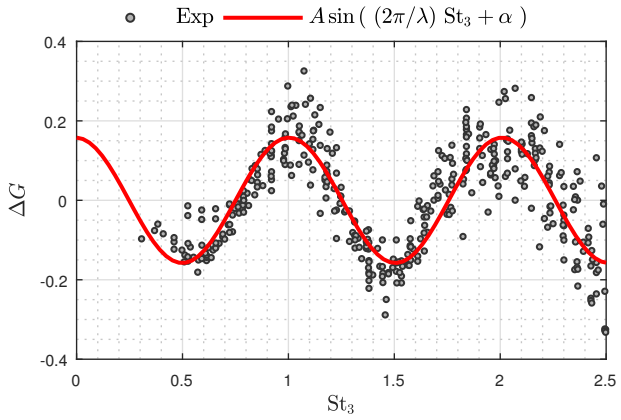

Figure 8: Low frequency modulations scaled by St_3. The red line is a sinusoidal curve fitted to the data. Since the data is already scaled by the appropriate Strouhal number $\lambda \approx 1$, otherwise it can be used to compute the wavelength and thus extract the value of τ_3.

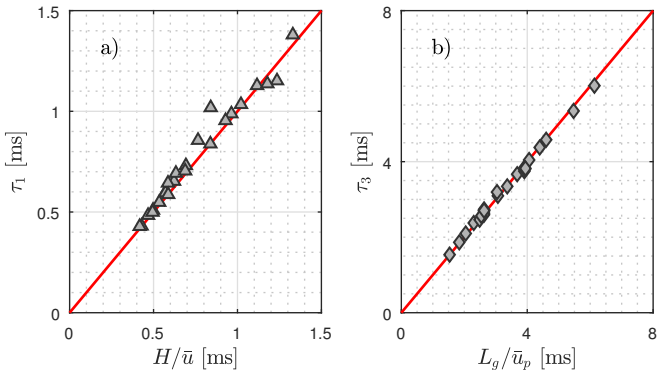

Figure 9: time-delays vs scaling parameters. The markers are the values of the time-delays obtained from the fitting procedure. The red line is a straight line with unit slope.

to:

$$1 = g_1 \exp\left(-\frac{1}{2}\beta_1^2\sigma_1^2\right) + g_2 \exp\left(-\frac{1}{2}\beta_2^2\sigma_2^2\right). \tag{21}$$

For numerical reasons it is convenient to define the gain of the first distribution as a function of the second one:

$$g_1 = \exp\left(\frac{1}{2}\beta_1^2\sigma_1^2\right)\left(1 - g_2 \exp\left(-\frac{1}{2}\beta_2^2\sigma_2^2\right)\right). \tag{22}$$

This constraint is ensured only in the third step of the fitting process, effectively eliminating one of the variables (g_1) from the fitting procedure.

3.4. Analysis of DTL model parameters

After obtaining the model parameters from the fitting procedure for the 25 cases, we proceed to analyse the nature of the time-delays.

Consider first the time-delay associated with the first distribution of the model (DTL_1). Figure 7 shows that the phase slopes and cut-off frequency characteristics of the 25 sets of experimental data collapse when scaled using the Strouhal number $St_1 = fH/\bar{u}$. Therefore by plotting τ_1 vs $H/\bar{u}$ one would expect a linear relationship with unit proportionality constant.

Figure 9a shows that this is exactly the case. Given that the markers closely follow the trend, one can conclude that the time-delay is given by:

$$\tau_1 = \frac{H}{\bar{u}}. \tag{23}$$

The small deviations may be associated with the way the flame height is computed.

On the other hand, Equation 20 states that the time-delay associated with the second distribution is composed of two time-delays: τ_1 (given in Equation 23) and τ_3. A key characteristic with respect to τ_3 is that when the bulk velocity is kept constant (e.g., cases 10-12) while other operating conditions are varied, its value remains constant. This implies that the time-delay is associated with a fixed length scale. After inspection of the combustor, it is found that this length (L_g) corresponds to the distance between the grub screws and the dump plane (see Figure 10). Therefore:

$$\tau_3 = \frac{L_g}{\bar{u}_p}, \tag{24}$$

where $\bar{u}_p$ is the bulk velocity in the pipe, which is approximately $\bar{u}_p = 4/7\bar{u}$. As with the first time-delay, Figure 9b confirms that for all the cases τ_3 is given by Equation 24. Associated with τ_3 a Strouhal number is defined such that $\mathrm{St}_3 = f\tau_3$ which scales the low frequency modulations and is independent of the flame height. This is shown in Figure 8, where the gain difference (defined in Equation 17) of the 25 cases is plotted against St_3. Using Equation 24 and 20 one can relate the wavelength of the modulations to physical quantities: $\lambda = 2\pi\bar{u}_p/L_g$. This implies that the location of the modulations is given by the bulk velocity and the distance of the grub screws from the dump plane.

To portray the difference between the two time-delays (and to demonstrate the accuracy of the model to capture these FTFs) the attention is placed on two different sets of experimental data

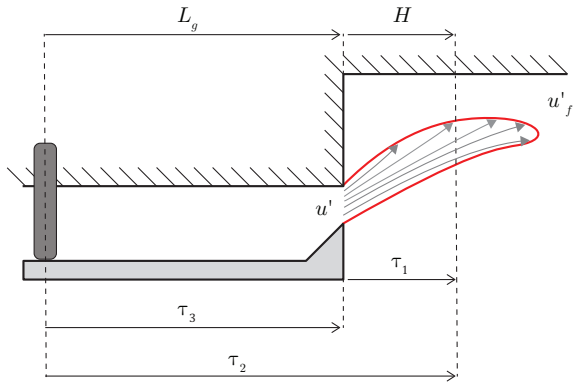

Figure 10: Schematic of an M flame. The red line denotes the flame front and the gray arrows represent the different paths that the velocity perturbations take to reach the flame front. Each path represents a different time-delay. Mean time-delays τ_1 and τ_2 and associated length scales L_g, and H are indicated on the schematic.

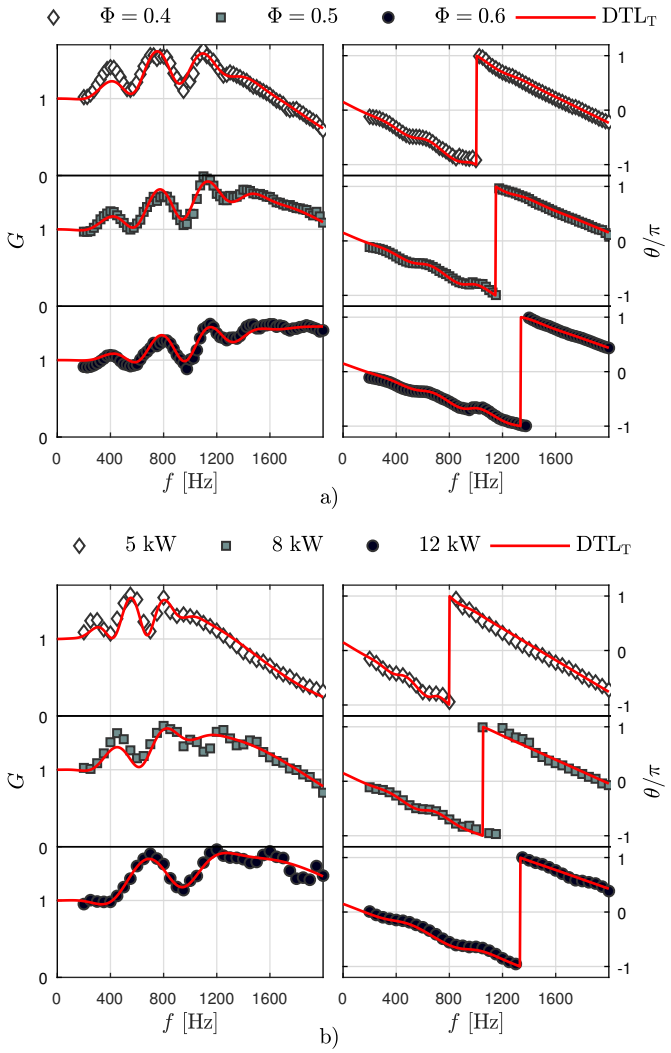

Figure 11: FTFs of pure hydrogen $P_{\mathrm{H}} = 1$, at different equivalence ratios and thermal powers. a) Case 10, case 11 and case 12 corresponding to an increase equivalence ratio at $\bar{u} = 30$ m/s and $P_{\mathrm{H}} = 1$. b) Case 3, case 6, and case 9 corresponding to an increase in thermal power for $P_{\mathrm{H}} = 1$ and $\Phi = 0.4$.

where pure hydrogen is used ($P_{\mathrm{H}} = 1$). The first set shown in Figure 11a corresponds to three FTFs where the equivalence ratio is increased while the bulk velocity is kept constant ($\bar{u} = 30$ m/s). Under these circumstances the flame length shortens because the flame speed increases. This implies that τ_1 gets smaller but τ_3 remains constant. Notice that the cut off frequency increases but that the periodicity and location of the modulations remain approximately constant. The second set shown in Figure 11b corresponds to three FTFs where the thermal power is increased at a constant equivalence ratio. Under these conditions both the flame length and bulk velocity increase. This causes τ_1 to become smaller because the bulk velocity grows faster than the flame length. τ_3 also becomes smaller. As before the cut-off frequency increases but to a lesser degree. Nonetheless, the modulations shift and stretch out in the frequency axis.

Having characterised each of the time-delays allows one to associate each of the distributions with the corresponding phys-

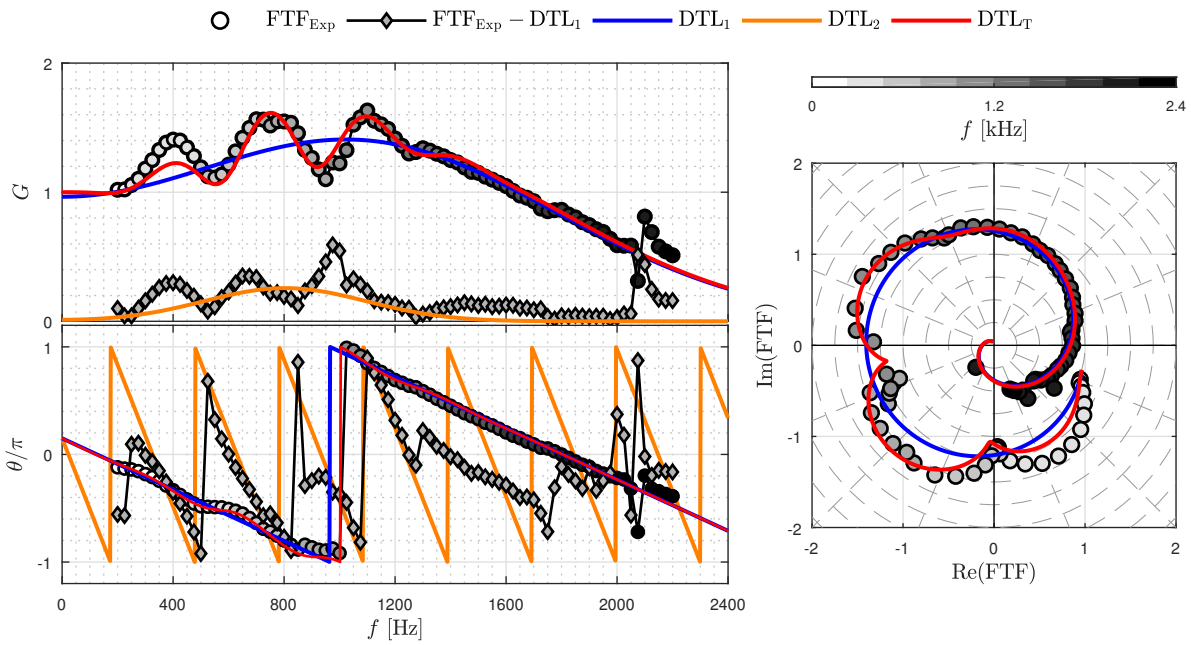

Figure 12: DTL model and its components corresponding to the FTF of case 5, $P_{\mathrm{H}} = 1$, $\Phi = 0.4$, and $P = 7$ kW.

ical mechanisms. Take as an example case 5 plotted in Figure 12. The first distribution (DTL$_1$) corresponds to the heat release fluctuations caused by the velocity fluctuations as they propagate from the dump plane until they reach the flame front. It presents a low pass filter behaviour and a short time-delay. The second distribution (DTL$_2$) corresponds to heat release fluctuations caused by the velocity fluctuations generated by vortex shedding at the grub screws. It has a band pass filter behaviour and a long time-delay. This behaviour is similar to that observed in swirl stabilized flames [21], where a trough in the gain appeared due to the destructive interference between a vorticity wave generated at the swirler and the acoustic velocity disturbances. For this case a similar conclusion is obtained: vortices shed from the grub screws generate large flame surface area fluctuations.

In general, this suggests that any type of upstream flow disturbances induced by geometry, can introduce modulations in the FTF. As long as the disturbances have a low pass or band pass filter behaviour they can be accurately represented by the distributed time lag model. In the following section a detailed cold flow analysis is performed to support the assumption that the second mechanism, DTL$_2$, is driven by vortex shedding from the grub screws.

3.5. Characterization of the second mechanism via cold flow measurements

Two sets of cold flow measurements are conducted. One measures the velocity at the burner exit and the second measures the velocity at different positions between the grub screws and the dump plane. For the first set of experiments a HWA is placed at the burner exit above one of the grub screws. The HWA is used to sample time series of unforced flow velocity u_{hw} in 5 min intervals, at 5 different bulk velocities. The time series are used to estimate the energy spectra $E_u = \int \left(u'_{\mathrm{hw}} * u'_{\mathrm{hw}}\right) \exp(j\omega t)\, \mathrm{d}t$ plotted in Figure 13. We observe that there is a peak in the spectra at all bulk velocities. The frequency at which the peaks are located increases with bulk velocity. In the inset of Figure 13 each spectra is normalized by the peak value and plotted against St$_3$. The collapse of this data with St$_3$, is an indication that the second mechanism is driven by vortex shedding. The corresponding Strouhal number based on the grub screw diameter (d_g) is $\mathrm{St}_{d_g} = 0.12$ and the range of Reynolds numbers is $\mathrm{Re}_{d_g} = [1200 - 7500]$.

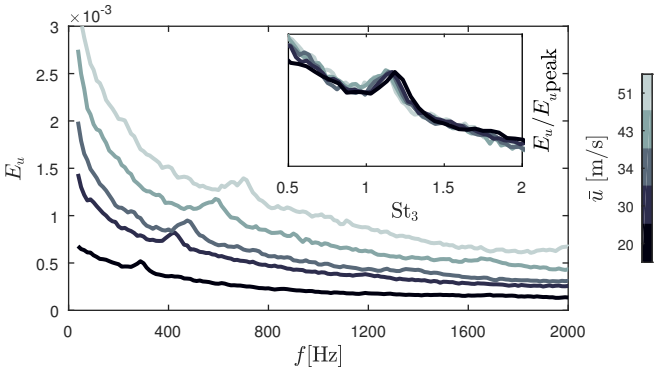

Figure 13: Energy spectra of the unforced flow at a range of bulk velocities. Peaks appear at St$_3$ ≈ 1.2 due to vortex shedding from the grub screws. This corresponds to $\mathrm{St}_{d_g} = f d_g/\bar{u}_p \approx 0.12$.

For the second set of experiments the bluff body is removed in order to fit the HWA inside the pipe. However, the center rod and the grub screws are left in, such that the forced flow experiences the same conditions as when measuring FTFs. For this set of experiments the forcing level and the bulk velocity in the

pipe are kept constant. The velocities measured by the MMM (u) and the HWA (u_{hw}) are sampled simultaneously at different downstream locations $L_h = \tilde{L}\, d_g$ with respect to the grub screws (see Figure 1 for an schematic). Figure 14 shows the magnitude and phase of the ratio $\hat{u}/\hat{u}_{hw}$ vs frequency at three different locations. Both quantities are computed in the same way as for the FTFs (Equation 2). Notice the presence of similar modulations that decay with the distance from the grub screw. These modulations are caused by the interference between the acoustic velocity and the velocity disturbances induced by vortex shedding from the grub screws. The time delay, being inversely proportional to the wavelength of the modulations, increases when the measurement point is further away from the grub screw. These measurements show that changing the position of the grub screws (varying L_g) has the same effect in the time delay as increasing the bulk velocity (as done above for the FTFs).

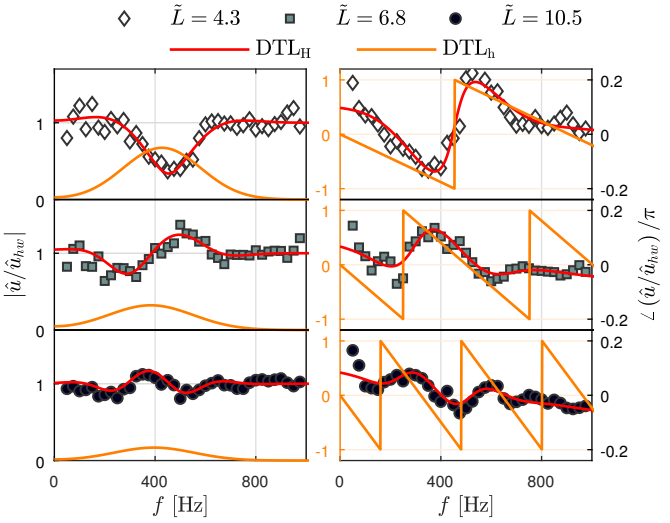

Figure 14: Magnitude and phase difference of the ratio $\hat{u}/\hat{u}_{\mathrm{hw}}$ at $\bar{u}_p = 13.7$ m/s. DTL$_{\mathrm{H}}$ (red lines) is used to capture the cold flow modulations between the velocity measured by the MMM and the velocity measured by HWA. This data set presents similar interference patterns as those observed in the FTFs.

To obtain more information from the measurements we fit two distributions DTL$_{\mathrm{H}}$ = DTL$_a$ + DTL$_{\mathrm{h}}$. The first distribution DTL$_a \approx 1$ is used to represent the fraction of velocities containing only the acoustic component. A small time delay is added to correct for the small phase deviation caused by uncertainty between the two measurements. The second distribution DTL$_h$ represents the fraction of velocities between the acoustic and induced velocities due to vortex shedding. Thus, the coefficients τ_h, g_h, β_h, and σ_h, describe the nature of the interfering mechanism, i.e., the frequency response of vortex shedding.

The fits (DTL$_{\mathrm{H}}$) are indicated by the red lines in Figure 14. The coefficients τ_h, g_h, σ_h, and β_h are shown in Figure 15. As expected, the time delay τ_h increases with L_h. The amplitude g_h decays exponentially with L_h. The frequency response given by σ_h and β_h remains constant. This indicates that the acoustic forcing locks on the natural shedding frequency of the grub screws [35]. These characteristics are taken into account

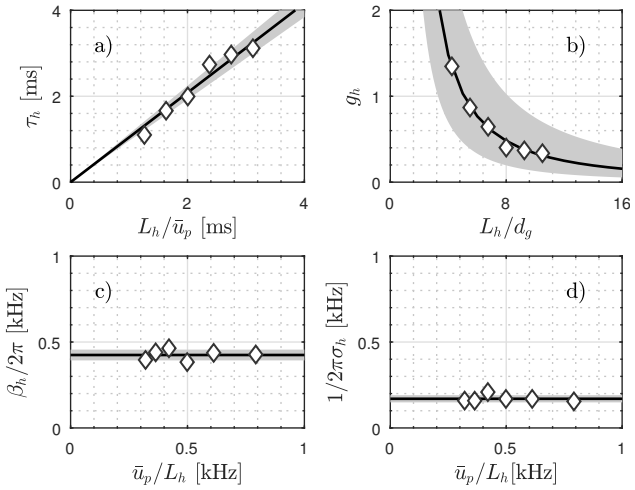

Figure 15: Parameters from DTL$_{\mathrm{H}}$ fitted to $\hat{u}/\hat{u}_{\mathrm{hw}}$ (red lines in Figure 14). The cold flow exhibits modulations with band-pass characteristics similar to those observed for the FTFs. $\tau_h \approx L_g/\bar{u}_p$, σ_h and β_h are approximately constant while g_h decays exponentially as indicated by the fitted black curves. Shaded regions indicate 95% confidence intervals.

when a generalized DTL model is developed later in the paper. The Strouhal number based on the grub screw diameter $\mathrm{St}_{d_g} = \beta_h d_g/(2\pi\bar{u}_p) = 0.13$ is close to the value obtained from the peaks of the spectra in Figure 13.

The analysis performed in this section provides further evidence that any type flow disturbances induced by the geometry upstream of the flame can introduce modulations in the FTF. Furthermore, the DTL model is able to capture the band pass filter characteristics of the second mechanism which in this case is centered at the shedding frequency given explicitly by $\beta_h/(2\pi)$ (a model parameter). Hence, the model used in this paper (Equation 15) gives an advantage compared to previous formulations of the DTL model [19].

In the following section we take advantage of the trends observed in both mechanisms in order to obtain a generalized DTL model for the measured FTFs.

4. Generalized distributed time lag model

Having analysed the two different mechanisms that constitute the distributed time lag model, we proceed to generalize the model. This enables the prediction of FTFs for a given flame height H, bulk velocity $\bar{u}$ and distance from the grub screws L_g. The challenge is to find a general expression for the gain parameters of the distributions (g_i, β_i, and σ_i) in terms of these inputs. General expressions for the phase parameters, i.e., time-delays, have already been deduced as seen in Figure 9.

In Figure 7 it is shown that the cut off characteristics collapse under the frequency scaling $H/\bar{u}$. Therefore it is convenient to define a cut-off frequency ω_c that scales with this reduced frequency. The value of ω_c is based on the following gain value of a single distribution:

$$|\mathrm{DTL}_1(\omega_c)| = \frac{1}{\sqrt{2}}\frac{g_1}{2}. \tag{25}$$

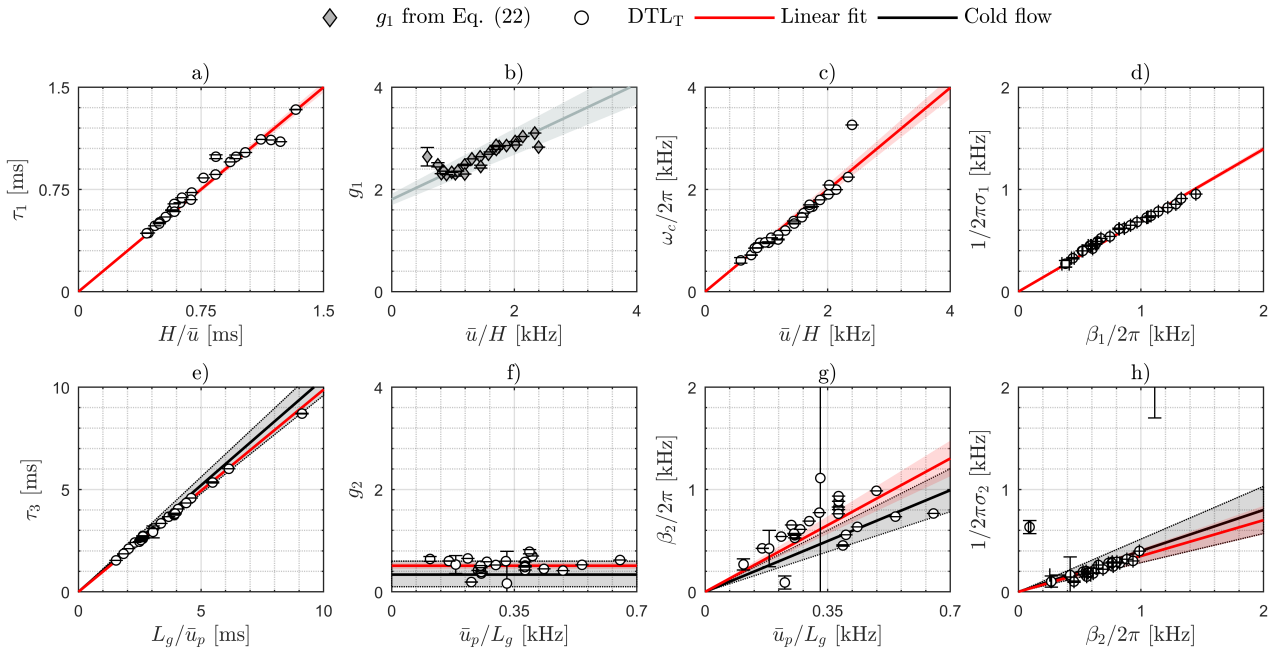

Figure 16: Dependence of the DTL model parameters with the flame and burner parameters H, $\bar{u}$ and L_g. Each marker corresponds to one of the 25 cases. The error bounds correspond to 3 standard deviations. The red lines correspond to linear fits of the data. Plot b) is only displayed for completeness, the actual value of g_1 is given by Equation 22. No linear regression is required for this variable. The black lines are estimates from the cold flow analysis. All shaded regions correspond to 95% confidence intervals.

Using this definition, combining it with Equation 15 and reorganizing the terms gives an implicit expression for the cut off frequency:

$$\omega_c = \beta + \frac{1}{\sigma_1}\sqrt{2\ln\left(\sqrt{2}\left(1+\exp\left(-2\sigma_1^2\beta_1\omega_c\right)\right)\right)}. \tag{26}$$

For all cases considered in this paper, $\exp(-2\sigma_1^2\beta_1\omega_c) \ll 1$, hence the previous equation can be approximated as:

$$\omega_c = \beta_1 + \frac{\sqrt{\ln(2)}}{\sigma_1}. \tag{27}$$

Since the cut off frequency depends on two parameters, another equation is required in order to generalize the model. The scaling used in section 3.3.1 and the results from section 3.5 suggest the following relationship between σ_i and β_i:

$$\frac{1}{\sigma_i} \propto \beta_i. \tag{28}$$

From the cold flow measurements we obtain that since L_g is constant $g_2 \approx$ constant and that the shedding frequency $\beta_2/(2\pi)$ increases linearly with bulk velocity:

$$\frac{\beta_2}{2\pi} \propto \frac{\bar{u}_p}{L_g}. \tag{29}$$

With all these definitions one can propose linear scalings for each of the distributions as shown in Figure 16 with their corresponding linear regression curve. The shaded regions indicate 95% confidence intervals on the fits. To generate this figure recall that each FTF corresponds to the mean of 40 different samples (see subsection 2.3). Therefore, in order to obtain the values of the model parameters instead of fitting them to the mean FTF values, they are fitted to each of the 40 samples. This enables the visualization of the experimental scatter given by the error bounds in the figure.

The first row in Figure 16 corresponds to the parameters of the first distribution all of which display a linear dependency as denoted by the fitted red line. The parameters of the second distribution are shown in the second row. For comparison, a black line and a gray shaded region have been added to represent the mean and scatter of the cold flow measurements. The parameters of the second distribution also display linear trends except for the gain g_2 which is shown to be constant with respect to $\bar{u}_p/L_g$. The shedding frequency $\beta_2/(2\pi)$ presents the most scatter. These data points seem to cluster along two lines corresponding to $\mathrm{St}_{d_g} \approx 0.11$ and $\mathrm{St}_{d_g} \approx 0.22$. A possible explanation is that both these lines correspond to the shedding frequency and the corresponding sub-harmonic. However, for consistency the linear fit (red line) is used to represent the trend for the generalized model.

By knowing the coefficients of the linear fits (red lines in Figure 16) one can predict the FTF at different operating points which have not been tested. At least two points are required in order to compute the regression curves. In order to increase accuracy it is desirable to choose operating points with a large separation between the values of $H/\bar{u}$ and similarly for the values of $L_g/\bar{u}_p$.

4.1. Performance of generalized DTL

As a matter of example, the generalized model is computed using two operating conditions. Then its performance in terms of precision and accuracy is studied in detail.

For the computation of the generalized DTL model case 7 ($P_{\mathrm{H}} = 1$, $\Phi = 0.4$, $P = 9$ kW) and case 15 ($P_{\mathrm{H}} = 0.3$, $\Phi = 0.7$, $P = 3$ kW) are used. Case 7 has values $H/\bar{u} = 0.50$ ms and $L_g/\bar{u}_p = 2.00$ ms, while case 15 has $H/\bar{u} = 1.72$ ms and $L_g/\bar{u}_p = 9.1$ ms. This ensures that the points used to obtain the regression curves are far apart from each other.

To quantify the performance of the generalized model it is useful to start by defining the different transfer functions:

- $\mathrm{FTF_{Sin}}$ corresponds to a single sample of the experimental FTF.
- $\mathrm{FTF_{Exp}}$ corresponds to the FTF obtained by averaging the 40 samples of experimental data.
- $\mathrm{DTL_T}$ corresponds to the FTF obtained by fitting a single sample of the experimental data.
- $\mathrm{DTL_G}$ corresponds to the FTF obtained from the generalized model by interpolation.

Then the relative error between the gain of two transfer functions, say $\mathrm{FTF_A}$ and $\mathrm{DTL_B}$ is defined by:

$$\epsilon^{G}_{\mathrm{A-B}} = 1 - \frac{|\mathrm{FTF_A}|}{|\mathrm{DTL_B}|} \tag{30}$$

A similar definition is given for the relative error between the phases ($\epsilon^{\theta}_{\mathrm{A-B}}$). The three relevant relative errors used to study the accuracy and precision are:

1. $\epsilon_{\mathrm{Sin-Exp}}$, measures error due to experimental scatter.
2. $\epsilon_{\mathrm{Sin-T}}$, measures the error due to the fitting procedure.
3. $\epsilon_{\mathrm{Sin-G}}$, measures the error due to interpolation (regression model), the fitting procedure, the computation of flame height and experimental scatter.

The errors are computed for each of the 40 samples at all measured frequencies. The resulting arrays of relative error are shown as histograms in Figure 17 for case 5 ($P_{\mathrm{H}} = 1$, $\Phi = 0.4$, $P = 7$ kW). The errors take approximately the shape of a Gaussian probability density function (PDF) with S as the standard deviation and μ as the mean value. The metrics S and μ represent precision and accuracy respectively and are computed directly from the errors listed above for both the gain and the phase. The errors of $\mathrm{DTL_G}$ and $\mathrm{FTF_{Exp}}$ can be visualized in Figure 18. The dark gray shaded region corresponds to a normally distributed scatter of 3% in each of the parameters around the curve given by $\mathrm{DTL_G}$. The light gray shaded region corresponds to 3 times the standard deviation of the 40 samples. As it can be seen the generalized model predicts the FTF well within the uncertainty bounds of the experimental scatter.

To get an idea about the order of magnitude that each source of error (experimental scatter, fitting procedure, interpolation) contributes to the generalized model, S and μ are compared between the three computed errors ($\epsilon_{\mathrm{Sin-Exp}}$, $\epsilon_{\mathrm{Sin-T}}$, and $\epsilon_{\mathrm{Sin-G}}$).

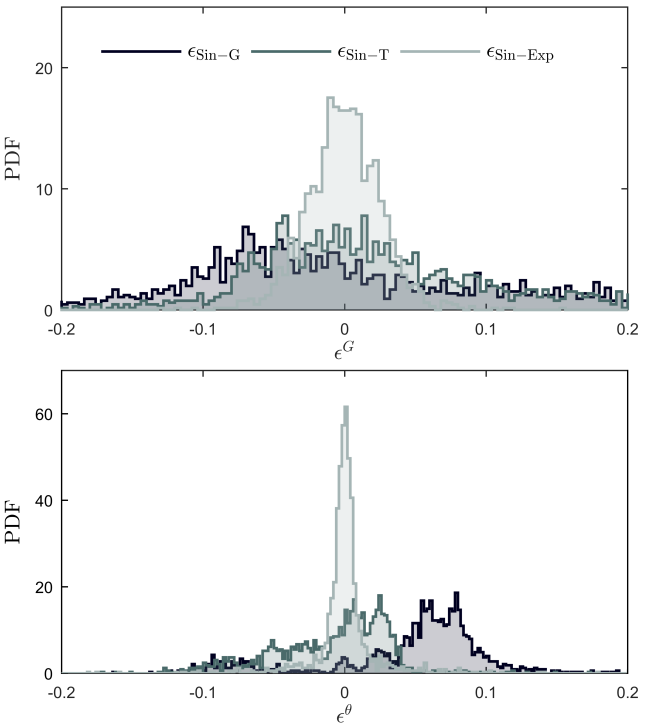

Figure 17: Histogram of relative errors in the gain ϵ^G and in the phase ϵ^θ for case 5 ($P_{\mathrm{H}} = 1$, $\Phi = 0.4$, $P = 7$ kW)

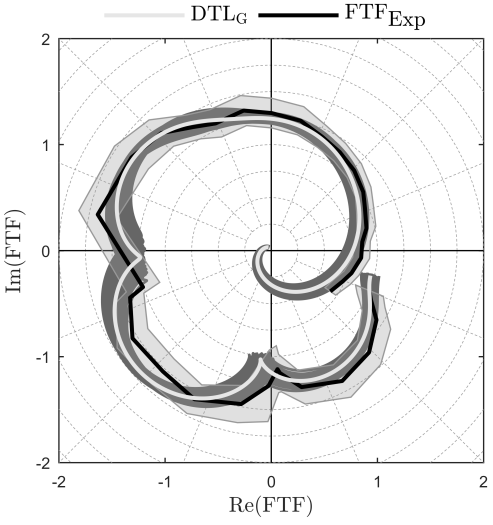

Figure 18: $\mathrm{DTL_G}$ and $\mathrm{FTF_{Exp}}$ for case 5 ($P_{\mathrm{H}} = 1$, $\Phi = 0.4$, $P = 7$ kW) plotted as complex numbers. The dark gray shaded region shows a normally distributed uncertainty of 3% imposed on all input parameters of $\mathrm{DTL_G}$. The light gray shaded region corresponds to the error bounds given by 3 standard deviations of the experimental measurements.

First the relative errors in the prediction of the gain are considered. The experimental scatter has a precision of $\mu = 0.00$ and an accuracy of $S = 0.02$. The fitting procedure $\mathrm{DTL_T}$ has a precision of $\mu = 0.01$ and an accuracy of $S = 0.07$. The generalized model $\mathrm{DTL_G}$ predicts the gain with a precision of

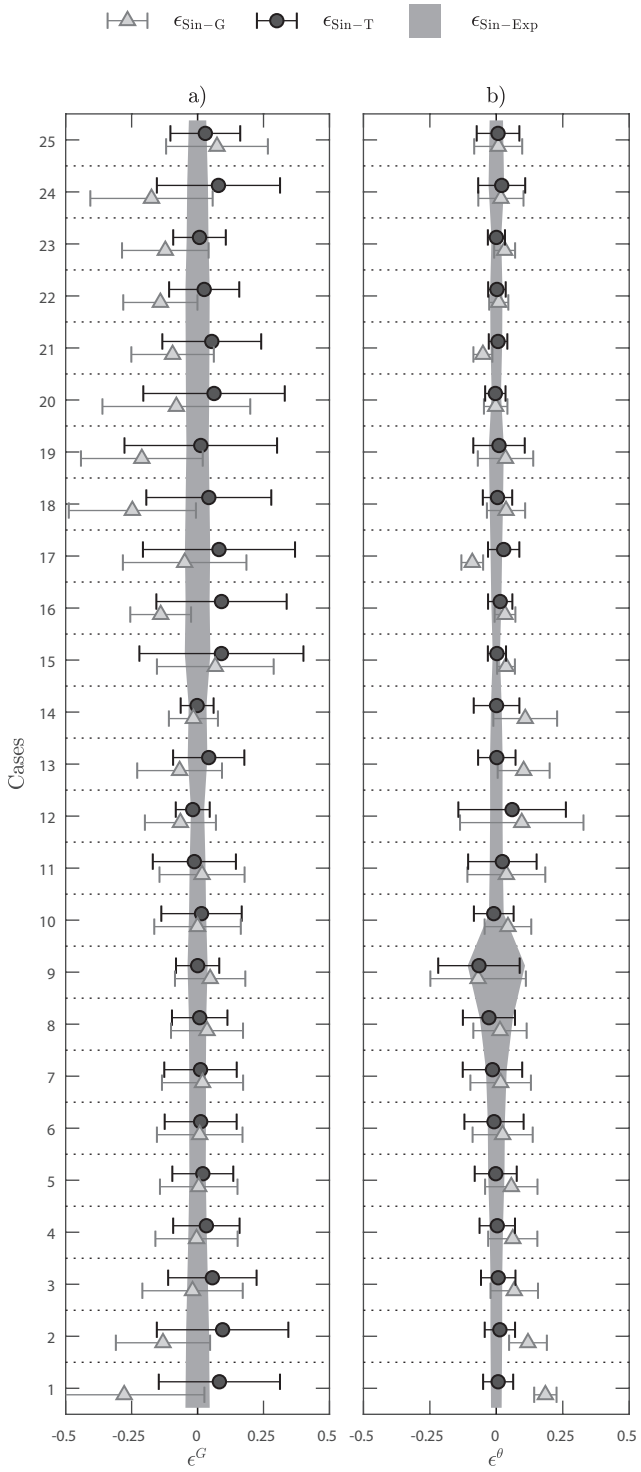

Figure 19: Summary of the performance of the generalized DTL model. Accuracy (μ) and precision (S) computed for the gain a) and phase b) for all three errors ($\epsilon_{\text{Sin-Exp}}$, $\epsilon_{\text{Sin-T}}$, and $\epsilon_{\text{Sin-G}}$). Error bounds are $\pm 1.3S$.

$\mu = 0.04$ and an accuracy of $S = 0.09$. Notice that the errors due to the fitting procedure and the experimental scatter are included in DTL_G, therefore it is expected that the values of μ and

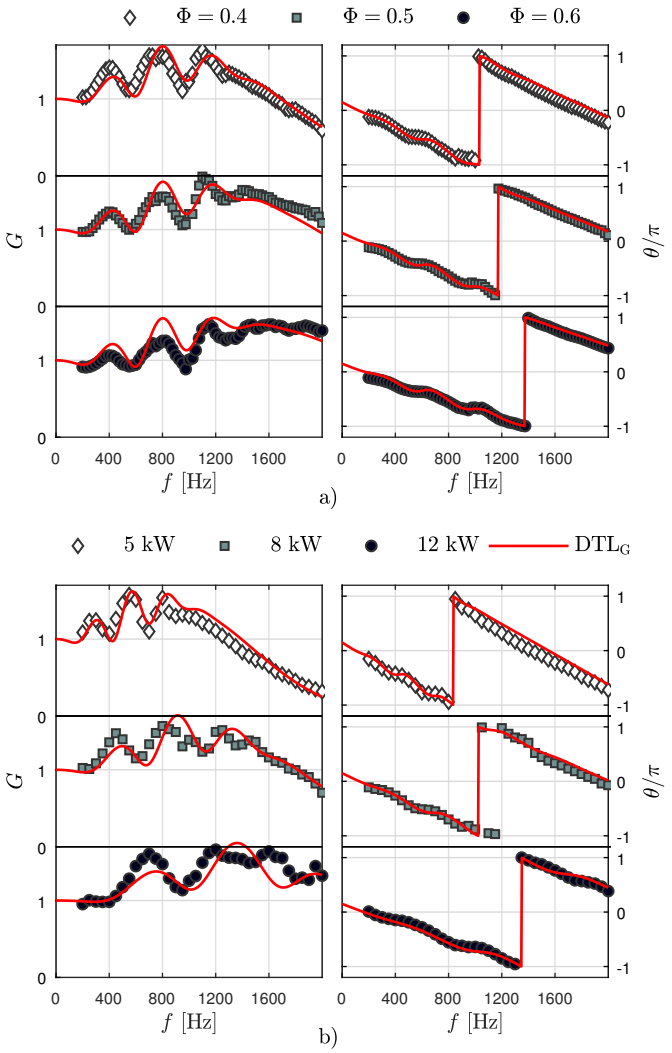

Figure 20: FTF_Exp and predicted FTFs by DTL_G. a) Case 10, case 11 and case 12 corresponding to an increase equivalence ratio at $\bar{u} = 30$ m/s and $P_\text{H} = 1$. b) Case 3, case 6, and case 9 corresponding to an increase in thermal power for $P_\text{H} = 1$ and $\Phi = 0.4$. All cases correspond to the same fitted cases shown in Figure 11.

S from the generalized model to be higher. Furthermore, one can notice that in terms of accuracy all estimates are of same order of magnitude and if one adds S computed from $\epsilon_{\text{Sin-Exp}}$ and $\epsilon_{\text{Sin-T}}$, one gets roughly the same value as computed from $\epsilon_{\text{Sin-G}}$. This indicates that the generalized model predicts the gain to a similar degree of precision as the fitting procedure and the experimental scatter. A similar conclusion can be made by considering the errors from the phase. An estimation of the magnitude of the error for this case is $|\mu| < 0.1$ and $|S| < 0.1$ for the gain and $|\mu| < 0.05$ and $|S| < 0.05$ for the phase.

This procedure is repeated for all 25 cases where μ and S are computed for both the gain and the phase. The results are summarized in Figure 19 which shows ϵ^G and ϵ^θ for the three errors. The error bars correspond to a projection of the histograms displayed in Figure 17. The markers indicate the mean μ and the error bounds are computed as $\pm 1.3S$ which correspond to 80% confidence intervals given that the error is Gaussian distributed.

The shaded regions also correspond to 80% confidence intervals of the experimental scatter with $\mu = 0$ by definition. One can see that the accuracy of the fitting procedure is better than the accuracy of the generalized model as one would expect. However, the precision is in the same order of magnitude for both DTL_T and DTL_G and for most cases the value of $1.3S$ is less than 20%. The prediction of the phase is better than for the gain, mainly due to the lower values of the experimental scatter.

To get a better visual representation of the performance (Figure 19) DTL_G and FTF_{Exp} are presented for six cases as shown in Figure 20. The cases correspond to the same FTFs fitted in Figure 11. One can see that using only two cases to get the regression lines for the generalized model provides a good estimation of both the gain and the phase. The cut-off frequency varies significantly in Figure 20a and both the cut-off frequency and the periodicity of the modulations change significantly in Figure 20b. This shows that the generalized model is able to predict a great variety of cases provided that the scaling is approximately linear, as shown before. It is important to stress that the generalization of the method still needs to be tested for different flames shapes and conditions such as swirling flames.

5. Conclusions

Flame transfer function measurements of perfectly premixed, hydrogen-methane, bluff body stabilized, "M" flames are presented. The FTFs display peaks and troughs in both the gain and the phase which are shown to be a manifestation of the interaction of two velocity fluctuation mechanisms. The first mechanism corresponds to the velocity perturbations generated at the base of the flame as they propagate downstream to the flame front. It has a time-delay given by the flame height and the bulk velocity, i.e., $\tau_1 = H/\bar{u}$. The second mechanism corresponds to the vortices shed from the grub screws as they propagate downstream to the flame front as evidenced by the forced and unforced cold flow measurements. It has a time-delay given by the position of the grub screws, the bulk velocity in the pipe and the first time-delay, i.e., $\tau_2 = \tau_1 + L_g/\bar{u}_p$. It is shown that a Strouhal number based on τ_1 collapses the cut off frequency characteristics of the 25 measured cases. On the other hand a Strouhal number based on the time-delay $\tau_3 = \tau_2 - \tau_1$ is shown to collapse all the peaks and troughs of the FTF.

A distributed time lag model based on the impulse response of each of the mechanisms is developed. It builds from previous models found in literature which consider two normal distributions of time-delays. The new model introduces a modulating term which shifts the peak of the distribution in the frequency space. This allows a single distribution to capture excess gain and allows the second mechanism to behave as a band pass filter centred around the modulating frequency. The benefit of this is that mechanisms exhibiting a preferred frequency, such as vortex shedding can easily be identified by analysing the model parameters. The new model is able to capture all the characteristics of the FTFs and the cold flow in detail.

Finally a generalized form of the distributed time lagged model is developed. This model takes as an input the bulk velocity and the flame height and predicts the corresponding FTF based on interpolation of the model parameters. The performance of the model is tested showing good predicting capabilities in terms of precision and accuracy. However, the model has only been used in M flames. The behaviour is expected to be different for V flames, conical flames or swirled flames, which may require the model to be extended.

Acknowledgments

The authors would like to acknowledge financial support from the Norwegian Research Council, Project No.: 257579/E20. The authors would also like to thank Dr. Wolfgang Polifke for valuable comments on an early draft of the paper.

References

[1] T. C. Lieuwen, V. Yang, Combustion Instabilities In Gas Turbine Engines: Operational Experience, Fundamental Mechanisms, and Modeling, American Institute of Aeronautics and Astronautics, Reston ,VA, 2006.

[2] C. Klsheimer, H. Bchner, Combustion dynamics of turbulent swirling flames, Combustion and Flame 131 (2002) 70–84.

[3] D. Durox, T. Schuller, N. Noiray, S. Candel, Experimental analysis of nonlinear flame transfer functions for different flame geometries, Proceedings of the Combustion Institute 32 (2009) 1391–1398.

[4] K. T. Kim, J. G. Lee, B. D. Quay, D. A. Santavicca, Response of partially premixed flames to acoustic velocity and equivalence ratio perturbations, Combustion and Flame 157 (2010) 1731–1744.

[5] P. Palies, D. Durox, T. Schuller, S. Candel, Nonlinear combustion instability analysis based on the flame describing function applied to turbulent premixed swirling flames, Combustion and Flame 158 (2011) 1980–1991.

[6] A. Kaufmann, F. Nicoud, T. Poinsot, Flow forcing techniques for numerical simulation of combustion instabilities, Combustion and Flame 131 (2002) 371–385.

[7] T. Schuller, D. Durox, S. Candel, A unified model for the prediction of laminar flame transfer functions: comparisons between conical and V-flame dynamics, Combustion and Flame 134 (2003) 21–34.

[8] W. Polifke, C. Lawn, On the low-frequency limit of flame transfer functions, Combustion and Flame 151 (2007) 437–451.

[9] A. P. Dowling, A kinematic model of a ducted flame, Journal of Fluid Mechanics 394 (1999) 51–72.

[10] M. Fleifil, A. M. Annaswamy, Z. A. Ghoneim, A. F. Ghoniem, Response of a laminar premixed flame to flow oscillations: A kinematic model and thermoacoustic instability results, Combustion and Flame 106 (1996) 487–510.

[11] L. Crocco, Aspects of Combustion Stability in Liquid Propellant Rocket Motors Part I: Fundamentals. Low Frequency Instability With Monopropellants, Journal of the American Rocket Society 21 (1951) 163–178.

[12] T. Sattelmayer, Influence of the Combustor Aerodynamics on Combustion Instabilities From Equivalence Ratio Fluctuations, Journal of Engineering for Gas Turbines and Power 125 (2003) 11–19.

[13] W. Polifke, J. Kopitz, A. Serbanoviv, Impact of the fuel time lag distribution in elliptical premix nozzles on combustion stability, in: 7th AIAA/CEAS Aeroacoustics Conference and Exhibit, American Institute of Aeronautics and Astronautics, Reston, Virigina, 2001, pp. 1–11.

[14] P. Preetham, S. Hemchandra, T. Lieuwen, Forced Response of Premixed Flames: Effect of Flow Non-uniformity, in: 46th AIAA Aerospace Sciences Meeting and Exhibit, American Institute of Aeronautics and Astronautics, 2008.

[15] A. Huber, W. Polifke, Dynamics of Practical Premixed Flames, Part II: Identification and Interpretation of CFD Data, International Journal of Spray and Combustion Dynamics 1 (2009) 229–249.

[16] R. S. Blumenthal, P. Subramanian, R. I. Sujith, W. Polifke, Novel perspectives on the dynamics of premixed flames, Combustion and Flame 160 (2013) 1215–1224.

[17] B. Schuermans, V. Bellucci, F. Guethe, F. Meili, P. Flohr, C. O. Paschereit, A Detailed Analysis of Thermoacoustic Interaction Mechanisms in a Turbulent Premixed Flame, in: Volume 1: Turbo Expo 2004, ASME, Vienna, Austria, 2004, pp. 539–551.
[18] W. Polifke, Black-box system identification for reduced order model construction, Annals of Nuclear Energy 67 (2014) 109–128.
[19] T. Komarek, W. Polifke, Impact of Swirl Fluctuations on the Flame Response of a Perfectly Premixed Swirl Burner, Journal of Engineering for Gas Turbines and Power 132 (2010).
[20] M. T. Szedlmayer, B. D. Quay, J. Samarasinghe, A. De Rosa, J. G. Lee, D. A. Santavicca, Forced Flame Response of a Lean Premixed Multi-Nozzle Can Combustor, in: Volume 2: Combustion, Fuels and Emissions, Parts A and B, ASME, Vancouver, British Columbia, Canada, 2011, pp. 883–891.
[21] P. Palies, D. Durox, T. Schuller, S. Candel, The combined dynamics of swirler and turbulent premixed swirling flames, Combustion and Flame 157 (2010) 1698–1717.
[22] M. Gatti, R. Gaudron, C. Mirat, T. Schuller, Effects of the Injector Design on the Transfer Function of Premixed Swirling Flames, American Society of Mechanical Engineers, 2017, pp. V04AT04A054–V04AT04A054.
[23] M. Gatti, R. Gaudron, C. Mirat, L. Zimmer, T. Schuller, A Comparison of the Transfer Functions and Flow Fields of Flames With Increasing Swirl Number, American Society of Mechanical Engineers, 2018, pp. V04BT04A003–V04BT04A003.
[24] M. Gatti, R. Gaudron, C. Mirat, L. Zimmer, T. Schuller, Impact of swirl and bluff-body on the transfer function of premixed flames, Proceedings of the Combustion Institute 37 (2019) 5197–5204.
[25] P. R. Alemela, D. Fanaca, C. Hirsch, T. Sattelmayer, B. Schuermans, Determination and Scaling of Thermo Acoustic Characteristics of Premixed Flames, International Journal of Spray and Combustion Dynamics 2 (2010) 169–198.
[26] K. T. Kim, D. A. Santavicca, Generalization of Turbulent Swirl Flame Transfer Functions in Gas Turbine Combustors, Combustion Science and Technology 185 (2013) 999–1015.
[27] J. R. Dawson, N. A. Worth, Flame dynamics and unsteady heat release rate of self-excited azimuthal modes in an annular combustor, Combustion and Flame 161 (2014) 2565–2578.
[28] N. A. Worth, J. R. Dawson, Self-excited circumferential instabilities in a model annular gas turbine combustor: Global flame dynamics, Proceedings of the Combustion Institute 34 (2013) 3127–3134.
[29] B. Higgins, M. Q. McQuay, F. Lacas, J. C. Rolon, N. Darabiha, S. Candel, Systematic measurements of OH chemiluminescence for fuel-lean, high-pressure, premixed, laminar flames, Fuel 80 (2001) 67–74.
[30] R. Balachandran, B. O. Ayoola, C. F. Kaminski, A. P. Dowling, E. Mastorakos, Experimental investigation of the nonlinear response of turbulent premixed flames to imposed inlet velocity oscillations, Combustion and Flame 143 (2005) 37–55.
[31] B. Schuermans, F. Guethe, D. Pennell, D. Guyot, C. O. Paschereit, Thermoacoustic Modeling of a Gas Turbine Using Transfer Functions Measured Under Full Engine Pressure, Journal of Engineering for Gas Turbines and Power 132 (2010) 111503.
[32] A. F. Seybert, D. F. Ross, Experimental determination of acoustic properties using a twomicrophone randomexcitation technique, The Journal of the Acoustical Society of America 61 (1977) 1362–1370.
[33] B. D. Bellows, M. K. Bobba, J. M. Seitzman, T. Lieuwen, Nonlinear Flame Transfer Function Characteristics in a Swirl-Stabilized Combustor, Journal of Engineering for Gas Turbines and Power 129 (2007) 954–961.
[34] C. J. Dasch, One-dimensional tomography: a comparison of Abel, onion-peeling, and filtered backprojection methods, Applied Optics 31 (1992) 1146.
[35] O. M. Griffin, M. S. Hall, ReviewVortex Shedding Lock-on and Flow Control in Bluff Body Wakes, Journal of Fluids Engineering 113 (1991) 526–537.